

High-Efficiency Photodynamic Antibacterial Activity of NH<sub>2</sub>-MIL-101(Fe)@MoS<sub>2</sub>/ZnO Ternary Composites

Junli Liu,\* Wenxia Cheng, Kaitao Zhang, Hui Liu, Junqi Li, John Tressel, and Shaowei Chen\*

Cite This: *ACS Appl. Bio Mater.* 2022, 5, 3912–3922

Read Online

ACCESS |



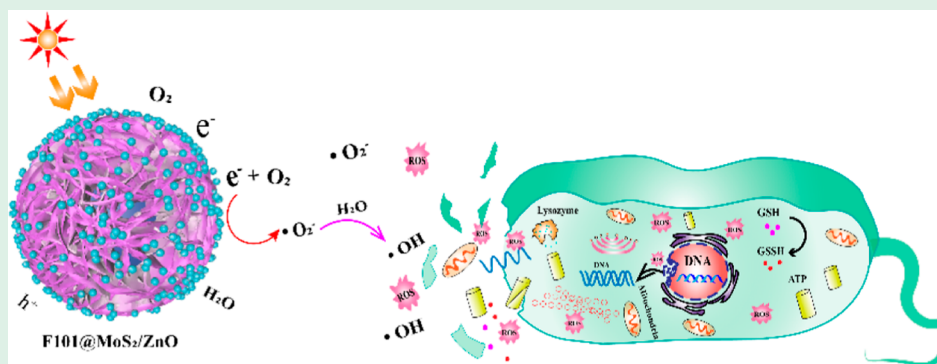
Metrics &amp; More



Article Recommendations



Supporting Information



**ABSTRACT:** Bacterial infections are a serious threat to human health, and the development of effective antibacterial agents represents a critical solution. In this study, NH<sub>2</sub>-MIL-101(Fe)@MoS<sub>2</sub>/ZnO ternary nanocomposites are successfully prepared by a facile wet-chemistry procedure, where MoS<sub>2</sub> nanosheets are grown onto the MIL-101 scaffold forming a flower-like morphology with ZnO nanoparticles deposited onto the surface. The ternary composites exhibit a remarkable sterilization performance under visible light irradiation toward both Gram-negative and Gram-positive bacteria, eliminating 98.6% of *Escherichia coli* and 90% of *Staphylococcus aureus* after exposure to visible light for 30 min, a performance markedly better than that with NH<sub>2</sub>-MIL-101(Fe)@MoS<sub>2</sub> binary composites and even more so than MoS<sub>2</sub> nanosheets alone. This is ascribed to the unique electronic band structure of the composites, where the separation of the photogenerated carriers is likely facilitated by the S-scheme mechanism in the NH<sub>2</sub>-MIL-101(Fe)@MoS<sub>2</sub> binary composites and further enhanced by the formation of a p–n heterojunction between MoS<sub>2</sub> and ZnO in the ternary composites. This interfacial charge transfer boosts the effective production of superoxide radicals by the reduction of oxygen, and the disproportionation reaction with water leads to the formation of hydroxyl radicals, as attested in spectroscopic and microscopic measurements. Results from this study highlight the significance of structural engineering of nanocomposites in the manipulation of the electronic band structure and hence the photodynamic activity.

**KEYWORDS:** NH<sub>2</sub>-MIL-101(Fe)@MoS<sub>2</sub>, photodynamic, antibacterial activity, Gram-positive, Gram-negative

## 1. INTRODUCTION

Bacterial infections pose a serious threat to human health.<sup>1,2</sup> Antibiotics are traditional remedies to treat bacterial infections, but long-term usage of antibiotics can cause bacteria to develop drug resistance.<sup>3–5</sup> In recent years, inorganic composites have been extensively studied as effective bactericidal agents,<sup>6,7</sup> and photodynamic and photothermal effects are the leading antibacterial mechanisms,<sup>8</sup> which can kill bacteria efficiently with minimal cytotoxicity and side effects.<sup>9,10</sup> Specifically, under photoirradiation, photosensitive materials can produce reactive species, which are known potent antimicrobial agents.<sup>11</sup> Concurrently, the sample temperature can be increased substantially and may impact cell membrane permeability<sup>12,13</sup> and enable reactive species to enter the bacterial cells and oxidize proteins and enzymes within the cells.<sup>14,15</sup> Such a performance is apparently dictated by the optoelectronic properties of the photocatalysts.

Molybdenum disulfide (MoS<sub>2</sub>) is a well-known p-type semiconductor that exhibits a two-dimensional lamellar structure and high electron mobility,<sup>16</sup> and the relatively narrow band gap (1.8 eV) allows for photoexcitation by photons within the ultraviolet to visible range,<sup>17,18</sup> a unique characteristic that has been exploited for solar energy conversion and photocatalysis.<sup>19,20</sup> Additionally, molybdenum disulfide has been confirmed to possess low cytotoxicity.<sup>21,22</sup> However, the low electron–hole separation efficiency of

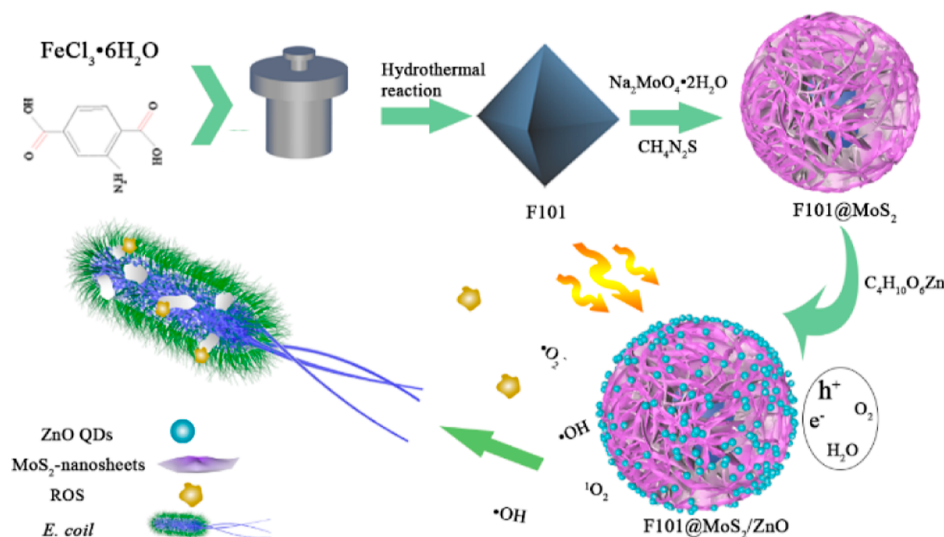
Received: May 12, 2022

Accepted: July 14, 2022

Published: August 3, 2022



### Scheme 1. Schematic Illustration of the Preparation of F101@MoS<sub>2</sub>/ZnO Nanocomposites and the Corresponding Antibacterial Activity



pristine MoS<sub>2</sub> greatly limits its photocatalytic performance.<sup>18</sup> This can be improved by the formation of p–n heterojunctions with an n-type semiconductor,<sup>16,23–25</sup> such as zinc oxide (ZnO), which has been known to be an excellent photocatalyst due to its high photosensitivity, low cost, controllable form, environmental nontoxicity, and chemical stability.<sup>26–29</sup>

Iron-containing metal–organic framework, NH<sub>2</sub>-MIL-101(Fe), is another photocatalytic material with a high surface area, strong absorption in the visible range, and robust structure, where the ligands can activate the metal cluster nodes under photoexcitation.<sup>30,31</sup> Notably, the electron-donating amine groups (–NH<sub>2</sub>) can enhance the photocatalytic activity and photostability of NH<sub>2</sub>-MIL-101(Fe) by boosting electron mobility and absorption in the visible light range.<sup>32</sup> Furthermore, the cavities within NH<sub>2</sub>-MIL-101(Fe) allow for efficient growth of MoS<sub>2</sub> nanosheets due to its adjustable pore size and abundant active groups (e.g., COOH, NH<sub>2</sub>, and OH).<sup>33,34</sup> Yet, there has been no report on the construction of NH<sub>2</sub>-MIL-101(Fe)@MoS<sub>2</sub>/ZnO nanocomposites.

In the present study, ternary NH<sub>2</sub>-MIL-101(Fe)@MoS<sub>2</sub>/ZnO nanocomposites are prepared via a facile hydrothermal procedure, where the unique photocatalytic activity leads to a high antibacterial efficiency toward both Gram-negative *Escherichia coli* and Gram-positive *Staphylococcus aureus*. As depicted in Scheme 1, NH<sub>2</sub>-MIL-101(Fe) is selected as the structural scaffold for the growth of MoS<sub>2</sub> nanosheets, producing flower-like NH<sub>2</sub>-MIL-101(Fe)@MoS<sub>2</sub> microspheres (denoted as F101@MoS<sub>2</sub>). Subsequently, ZnO quantum dots (QDs) are deposited onto the outer surface of F101@MoS<sub>2</sub> to produce ternary NH<sub>2</sub>-MIL-101(Fe)@MoS<sub>2</sub>/ZnO composites (denoted as F101@MoS<sub>2</sub>/ZnO). Remarkably, the resulting composites exhibit excellent antimicrobial activity, eliminating 98.6% of *E. coli* and 90% of *S. aureus* after exposure to visible light for 30 min, mostly due to the effective photocatalytic generation of superoxide and hydroxy radicals.

## 2. EXPERIMENTAL SECTION

**2.1. Chemicals.** Sodium molybdate (Na<sub>2</sub>MoO<sub>4</sub>·2H<sub>2</sub>O), thiourea, zinc acetate [Zn(OAc)<sub>2</sub>·2H<sub>2</sub>O], potassium hydroxide (KOH, AR, 99.5%), ferric chloride (FeCl<sub>3</sub>·6H<sub>2</sub>O, AR, 99%), 2-aminoterephthalic

acid, *N,N*-dimethylformamide (DMF, 99%), and glutaraldehyde were acquired from Macklin Co., Ltd (Shanghai, China). Propidium iodide (PI) and SYTO9 were purchased from Kailiqi Biopharma Technology Co., Ltd (Tianjin, China). Glutathione (GSH) and Tris–HCl buffer (C<sub>4</sub>H<sub>11</sub>NO<sub>3</sub>) were acquired from Macklin Biochemicals Co., Ltd. All reagents were used directly without additional purification.

**2.2. Synthesis of NH<sub>2</sub>-MIL-101(Fe).** NH<sub>2</sub>-MIL-101(Fe) was synthesized by following a procedure described previously.<sup>35</sup> In brief, 4.16 mmol of FeCl<sub>3</sub>·6H<sub>2</sub>O and 2.15 mmol of 2-aminoterephthalic acid were mixed into 40 mL of DMF under stirring for 40 min. The mixture was then heated at 110 °C for 24 h in a Teflon-lined reactor. The reddish-brown precipitate was collected via centrifugation and filtration, rinsed 3 times with a mixture of ethanol–water, and dried at 50 °C overnight. The product NH<sub>2</sub>-MIL-101(Fe) was abbreviated as F101.

**2.3. Synthesis of F101@MoS<sub>2</sub> Composites.** The F101@MoS<sub>2</sub> composite was synthesized by a simple one-step hydrothermal method. First, 0.3 g of Na<sub>2</sub>MoO<sub>4</sub>·2H<sub>2</sub>O and 0.5 g of thiourea were dispersed into 50 mL of ultrapure water under vigorous agitation for 40 min, into which was then added 1 g of the F101 prepared above under sonication for 1 h. The suspension was heated at 180 °C in a Teflon-lined reactor for 24 h. The black precipitate was collected by centrifugation, rinsed multiple times with a mixture of ethanol and water, and dried for 8 h at 60 °C, affording F101@MoS<sub>2</sub> composites.

**2.4. Synthesis of F101@MoS<sub>2</sub>/ZnO Composites.** To synthesize ternary F101@MoS<sub>2</sub>/ZnO composites, 0.48 g of Zn(OAc)<sub>2</sub>·2H<sub>2</sub>O and 0.24 g of KOH were added into 150 mL of ethanol under stirring for 20 min at 32 °C, into which was then added 0.4 g of F101@MoS<sub>2</sub> obtained above under sonication for 30 min. The solution was then placed in a flask and heated in an oil bath at 90 °C for 5 h. The produced black precipitate was collected by centrifugation, rinsed with a copious amount of water, and dried overnight at 50 °C, producing ternary F101@MoS<sub>2</sub>/ZnO composites.

**2.5. Structural Characterization.** The morphology of the samples was examined by transmission electron microscopy (TEM, F20 S-TWIN) and scanning electron microscopy (SEM, S4800, Japan). The elemental compositions were determined by energy-dispersive X-ray spectroscopy (EDS). X-ray diffraction (XRD, D/max 2200PC) patterns were acquired to investigate the crystalline structure. Raman spectra were collected to analyze the structure and composition of materials. X-ray photoelectron spectroscopy (AXIS ULTRA DLD) studies were carried out to evaluate the valence states and elemental compositions. Fluorescence spectroscopic measurements were conducted with an Omni PL spectrophotometer. Electron spin resonance (ESR, JEOL JES-FA200) measurements were

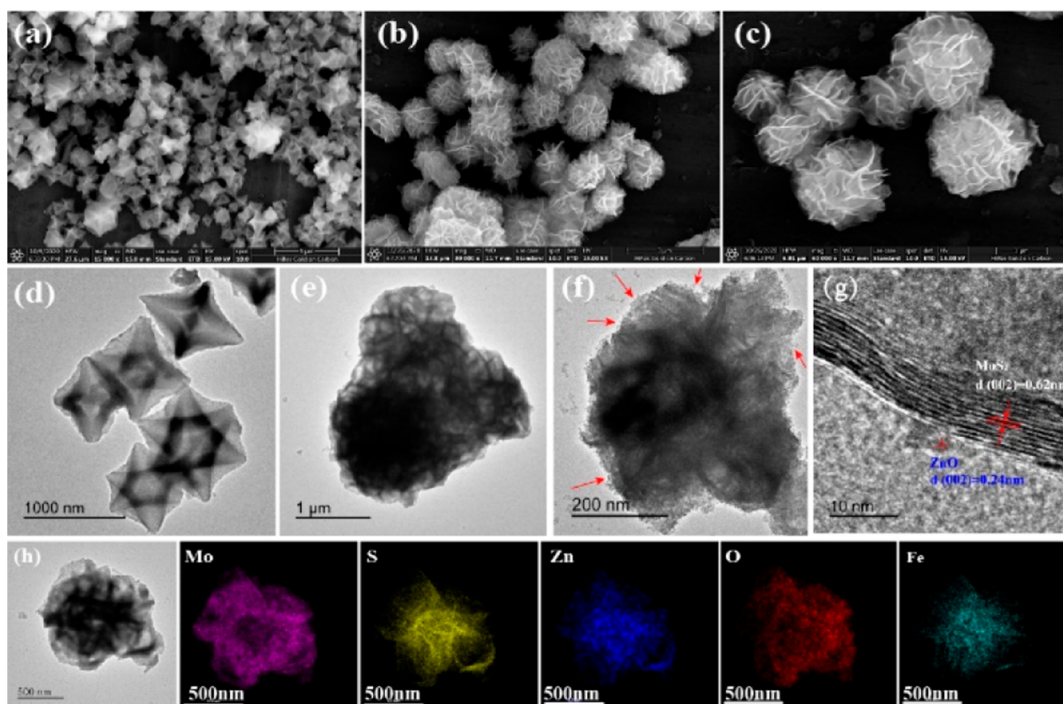


**Figure 1.** SEM images of (a) F101, (b) F101@MoS<sub>2</sub>, and (c) F101@MoS<sub>2</sub>/ZnO. TEM images of (d) F101, (e) F101@MoS<sub>2</sub>, and (f) F101@MoS<sub>2</sub>/ZnO. (g) HRTEM image of F101@MoS<sub>2</sub>/ZnO. (h) EDS images of F101@MoS<sub>2</sub>/ZnO.

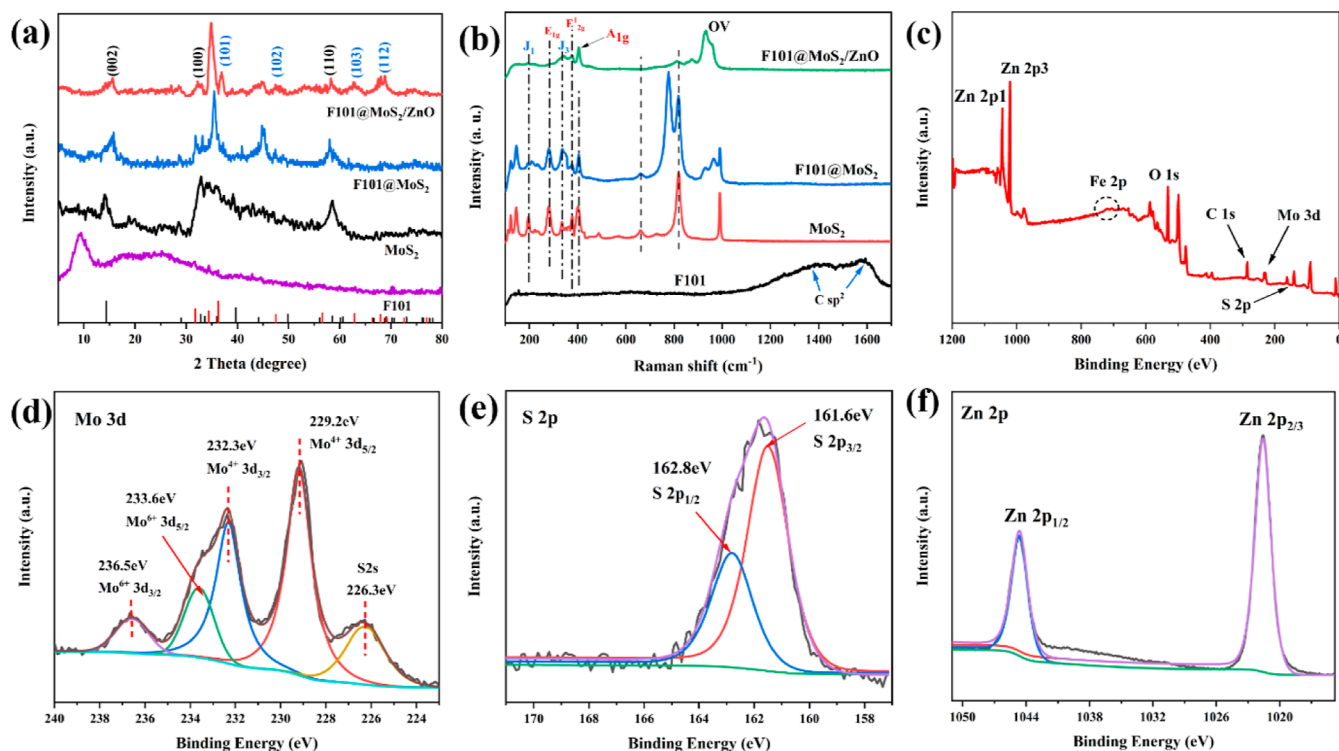


**Figure 2.** (a) XRD patterns and (b) Raman spectra of F101, MoS<sub>2</sub>, F101@MoS<sub>2</sub>, and F101@MoS<sub>2</sub>/ZnO composites. (c) XPS full spectrum and high-resolution scans of the (d) Mo 3d, (e) S 2p, and (f) Zn 2p electrons of F101@MoS<sub>2</sub>/ZnO composites.

carried out with 5-dimethyl pyrroline-1-oxide (DMPO) as the spin trap agent. Zeta potentials of the samples were measured with a Malvern NAMO-ZS instrument. Inductively coupled plasma-optical emission spectrometry (ICP-OES) measurements were conducted with an iCap 7400 analyzer.

**2.6. Electrochemical Studies.** In photoelectrochemical and electrochemical impedance spectroscopy measurements, a calculated

amount of the MoS<sub>2</sub>, F101@MoS<sub>2</sub>, and F101@MoS<sub>2</sub>/ZnO suspensions was dropcast onto the surface of a glassy-carbon electrode, which was used as the working electrode; a platinum wire as the counter electrode; and Ag/AgCl as the reference electrode, along with 0.1 M Na<sub>2</sub>SO<sub>4</sub> as the electrolyte.

The photocatalytic activity of the F101@MoS<sub>2</sub>/ZnO composite was evaluated by the degradation of methyl orange (MO, 10 mg L<sup>-1</sup>)



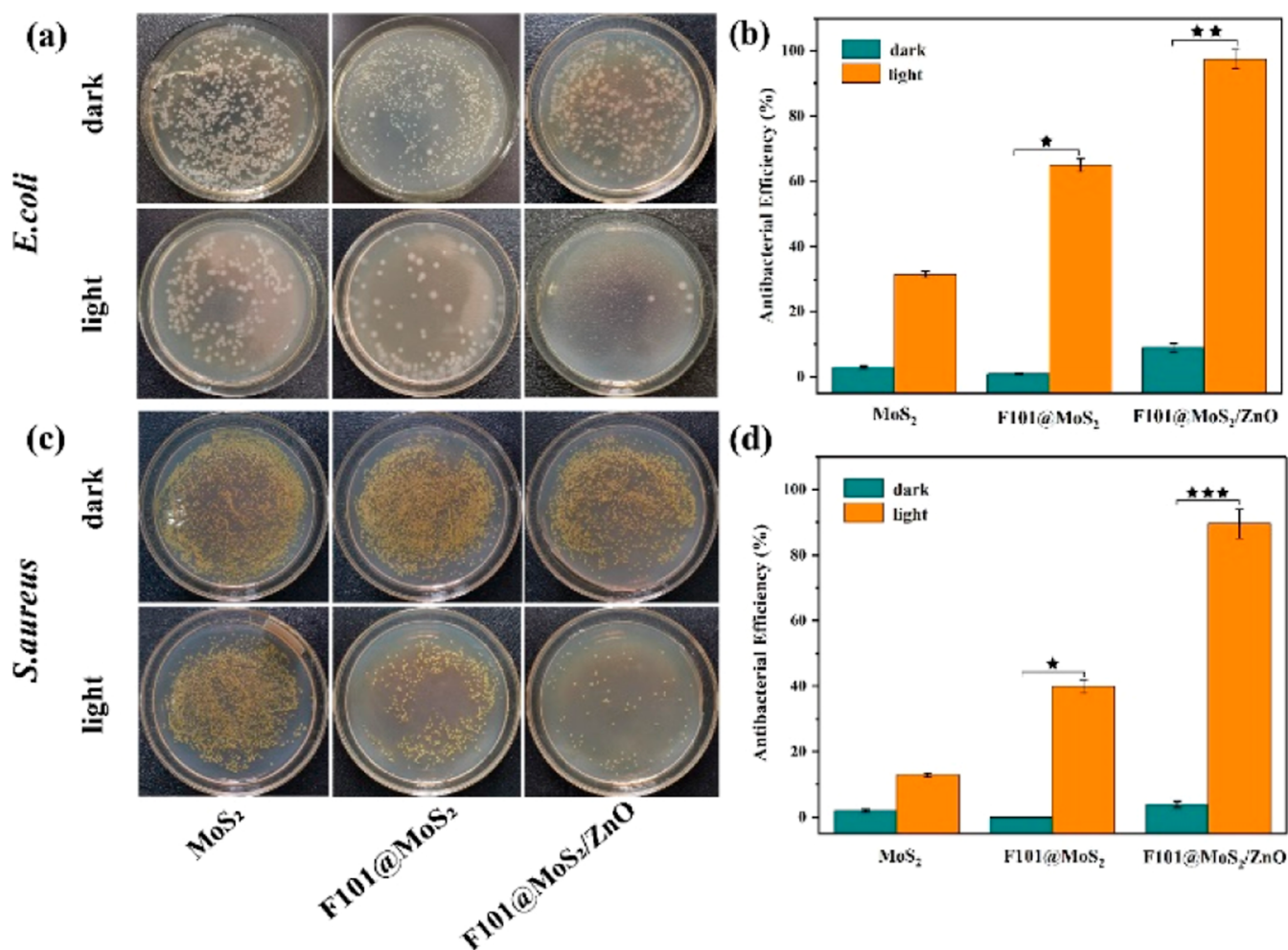


**Figure 3.** Photographs of the growth of (a) *E. coli* and (c) *S. aureus* after 30 min of treatment with MoS<sub>2</sub>, F101@MoS<sub>2</sub>, and F101@MoS<sub>2</sub>/ZnO under visible light irradiation (480–780 nm, 0.36 W cm<sup>-2</sup>) and in the dark. The corresponding antibacterial efficiency against (b) *E. coli* and (d) *S. aureus* (error:  $n = 3$ , \*\* $P < 0.01$ , \*\*\* $P < 0.001$ ).

under visible light irradiation (480 to 780 nm, 0.36 W cm<sup>-2</sup>). An aliquot of the MO solution was removed every 20 min to measure the optical absorbance of the supernatant with a UV–vis spectrophotometer.

**2.7. Ellman's Assay.** In Ellman's assay, 225  $\mu$ L of the composites prepared above and 225  $\mu$ L of GSH (1 mM) were dispersed into a 0.05 M phosphate buffer solution (PBS, pH = 8.5) and incubated for 10, 20, 30, and 40 min under simulated solar light irradiation, into which was then added 15  $\mu$ L of Ellman's reagent, 5,5'-dithio-bis-2-nitrobenzoic acid (DTNB, 0.1 mM), and 785  $\mu$ L of Tris–HCl (0.05 M, pH = 8.3). The supernatant was separated by centrifugation and injected into a 96-well microplate reader. The antioxidant performance of GSH was estimated by quantifying the absorbance loss of DTNB at 410 nm.

**2.8. Minimum Inhibitory Concentration.** The minimum inhibitory concentration (MIC) of MoS<sub>2</sub>, F101@MoS<sub>2</sub>, and F101@MoS<sub>2</sub>/ZnO composites against *E. coli* and *S. aureus* was measured using the 96-well cell culture dilution method. A single colony of *E. coli* or *S. aureus* was taken out of the broth medium (LB) and cultivated in the liquid LB medium for 12 h at 37 °C to obtain a fresh bacterial suspension. Subsequently, 5  $\mu$ L ( $1 \times 10^6$  CFU mL<sup>-1</sup>) of a fresh bacterial suspension and 5  $\mu$ L of liquid LB medium were inoculated into 96-well plates. Then, the sample was added to the 96-well plates and diluted with PBS into a series of concentration gradient solutions, with the final volume of the liquid at 100  $\mu$ L. The UV–vis absorption profiles of each group of samples were then recorded at a 10 min interval for 24 h by a microplate reader and the

absorbance at 600 nm was used to construct the growth curve, from which the corresponding MIC was determined.

**2.9. Photodynamic Antibacterial Performance.** *E. coli* or *S. aureus* (at OD = 0.1) and the nanocomposites at different concentrations were inoculated into a 5 mL centrifuge tube, shaken for 30 min to allow full contact between the bacteria and the composites, and irradiated under visible light (480–780 nm, 0.36 W cm<sup>-2</sup>). An aliquot (25  $\mu$ L) was taken out of the suspension and injected into the broth medium. After cultivation for 24 h, the number of colonies in the broth medium was used to estimate the bacterial survival rate. The antibacterial efficiency ( $\epsilon$ ) was calculated by using the formula,  $\epsilon = (I_0 - I_t)/I_0 \times 100\%$ , where  $I_0$  is the number of colonies in the control group and  $I_t$  is the number of colonies in the sample group.

**2.10. Fluorescent Staining of Bacteria.** The F101@MoS<sub>2</sub>/ZnO composites and bacterial suspension were placed into a 5 mL centrifuge tube under visible light photoirradiation for 30 min. The treated bacteria were rinsed with PBS and collected by centrifugation (6000 rpm), into which was added 50  $\mu$ L of PI (15  $\mu$ M) under shaking for 30 min. The PI-stained bacteria were rinsed with PBS before 50  $\mu$ L of SYTO9 (5  $\mu$ M) was added, and the suspension was subject to additional shaking for 30 min. The living and dead cells were examined through a fluorescence microscope, where dead cells marked with PI appeared red and live cells marked with SYTO9 appeared green.

**2.11. SEM Study of Bacterial Cells.** The effect of F101@MoS<sub>2</sub>/ZnO composites on the bacteria cell morphology was analyzed by SEM measurements. In brief, a bacteria suspension was treated with



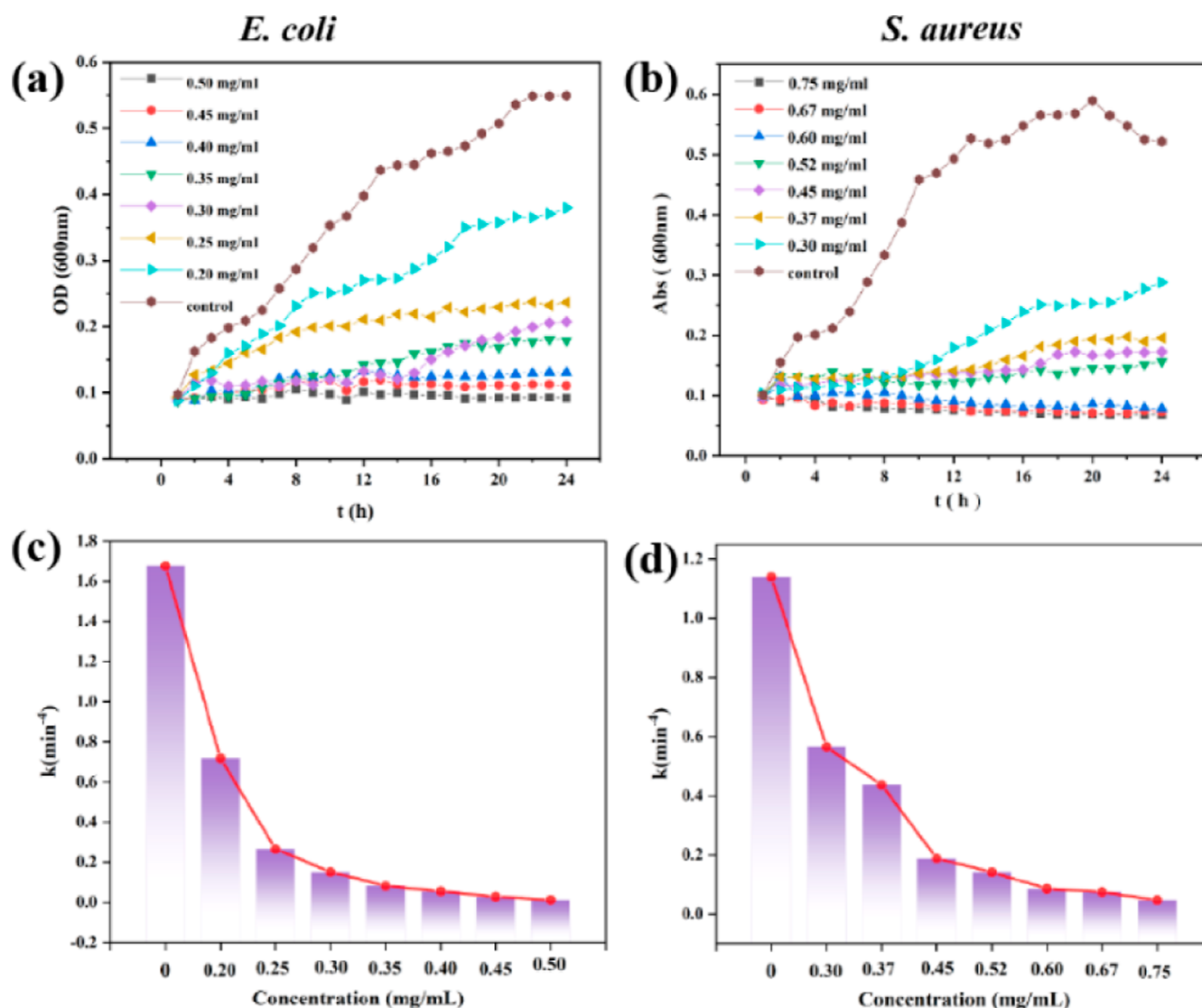


**Figure 4.** Growth curves of (a) *E. coli* and (b) *S. aureus* in the presence of F101@MoS<sub>2</sub>/ZnO at different concentrations (shown in figure legends). Growth rate constant of (c) *E. coli* and (d) *S. aureus* at different concentrations of F101@MoS<sub>2</sub>/ZnO.

the F101@MoS<sub>2</sub>/ZnO composites under visible light irradiation, collected by centrifugation, fixed for 2 h with 3% glutaraldehyde at 4 °C, and rinsed with PBS. Then, a different concentration of ethanol (25, 50, 75, and 99%) was used to dehydrate the cells, which were vacuum-dried for 4 h and sputter-coated with a thin layer of gold prior to the acquisition of SEM images.

### 3. RESULTS AND DISCUSSION

**3.1. Structural Characterization.** The microscopic morphology and size of the as-prepared composites were first analyzed by SEM measurements. From Figure 1a, F101 can be seen to exhibit a smooth rhombohedral octahedron shape (ca. 0.5 μm in diameter), in accordance with results reported in the literature.<sup>36</sup> Such a shape was largely retained in the F101@MoS<sub>2</sub> composite except that the surface became markedly roughened and decorated with a number of petals that are most likely MoS<sub>2</sub> nanosheets (Figure 1b). The formation of such a flower-like microsphere morphology (about 1 μm in diameter) was likely due to the high surface area and plentiful active sites of F101 for the growth of MoS<sub>2</sub> nanosheets<sup>33</sup> and driven by the electrostatic interaction between the positively charged F101 and negatively charged MoS<sub>2</sub>, as manifested in

the zeta potential ( $\zeta$ ) measurements (Figure S1). Further deposition of ZnO QDs onto F101@MoS<sub>2</sub>, which is also likely driven by electrostatic interactions (Figure S1), did not alter the material morphology, as evidenced in the SEM image of the F101@MoS<sub>2</sub>/ZnO composite in Figure 1c, probably due to the small size of the ZnO QDs (8–10 nm in diameter, Figure S2).

In TEM measurements, F101 can be seen to exhibit a diameter of approximately 500 nm (Figure 1d), consistent with results from SEM measurements (Figure 1a). The F101@MoS<sub>2</sub> (Figure 1e) and F101@MoS<sub>2</sub>/ZnO composites (Figure 1f) show a flower-like microsphere structure with an average size of 1 μm, where tiny ZnO QDs can be found to attach to the outer surface of F101@MoS<sub>2</sub>, as highlighted by the red arrows (Figures 1f and S2). From the HRTEM image in Figure 1g, the F101@MoS<sub>2</sub>/ZnO composite can be seen to show two sets of well-defined lattice fringes with an interplanar spacing of 0.62 and 0.24 nm due to the MoS<sub>2</sub> (002) and ZnO (101) crystal planes,<sup>37,38</sup> respectively; ZnO QDs are indeed attached onto the MoS<sub>2</sub> surface. In EDS measurements (Figure 1h), one can see that the elements of Mo, S, Zn, O, and Fe are

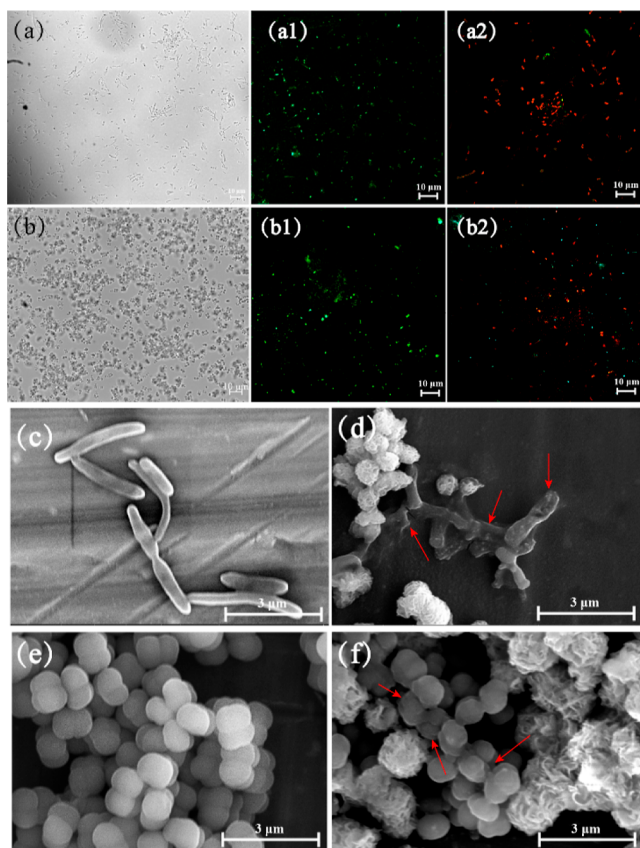


**Figure 5.** (a) Optical microscope image of *E. coli*. Fluorescence microscopic image of *E. coli* (a1) before and (a2) after visible light irradiation with F101@MoS<sub>2</sub>/ZnO composite for 20 min. (b) Optical microscope image of *S. aureus*. Fluorescence microscopic image of *S. aureus* (b1) before and (b2) after visible light irradiation with F101@MoS<sub>2</sub>/ZnO composite for 20 min. SEM images of *E. coli* (c) before and (d) after photoirradiation with F101@MoS<sub>2</sub>/ZnO for 20 min. SEM images of *S. aureus* (e) before and (f) after photoirradiation with F101@MoS<sub>2</sub>/ZnO for 20 min. Scale bars are (a–b2) 10 μm and (c–f) 3 μm.

uniformly distributed within the F101@MoS<sub>2</sub>/ZnO composite. These results confirm the successful preparation of ternary F101@MoS<sub>2</sub>/ZnO composites.

The XRD patterns of the sample series are shown in Figure 2a. F101 (purple curve) exhibits no clear diffraction peaks (except for the two broad peaks at  $2\theta = 9.2$  and  $25^\circ$ ),<sup>39,40</sup> suggestive of a mostly amorphous structure. For the F101@MoS<sub>2</sub> composite (blue curve), a series of new diffraction peaks emerged at  $2\theta = 14.3$ ,  $32.8$ , and  $58.5^\circ$ , which can be assigned to the (002), (100), and (110) crystal planes of MoS<sub>2</sub> (PDF# card no. 73-1508) (black curve), respectively.<sup>41</sup> In the F101@MoS<sub>2</sub>/ZnO composite, on top of the diffraction features of F101 and MoS<sub>2</sub>, additional diffraction peaks can be resolved at  $2\theta = 36.3$ ,  $47.5$ ,  $63.1$ , and  $67.9^\circ$ , corresponding to the (101), (102), (103), and (112) planes of ZnO (PDF# card no. 36-1451). This, again, confirms the successful preparation of the F101@MoS<sub>2</sub>/ZnO ternary composite.

Further structural insights are obtained from Raman spectroscopic measurements (Figure 2b). F101 (black curve) can be seen to exhibit two broad bands at  $1396$  and  $1584\text{ cm}^{-1}$ , arising from sp<sup>2</sup> carbon vibrations.<sup>36</sup> The MoS<sub>2</sub> shows three characteristic peaks at  $280.8$ ,  $376.5$ , and  $404.7\text{ cm}^{-1}$  due to the E<sub>1g</sub>, E<sub>2g</sub>, and A<sub>1g</sub> longitudinal phonon modes of 2H-MoS<sub>2</sub> (red

curve), along with three additional peaks at  $195.4$ ,  $235.6$ , and  $335.7\text{ cm}^{-1}$  characteristic of the phonon modes of 1T-MoS<sub>2</sub>.<sup>42,43</sup> These vibrational features were all well-defined in F101@MoS<sub>2</sub> and F101@MoS<sub>2</sub>/ZnO. The latter also includes a peak at  $938\text{ cm}^{-1}$  due to the oxygen vacancy on the surface of ZnO QDs.<sup>44,45</sup> Taken together, these results further confirm the successful preparation of the F101@MoS<sub>2</sub>/ZnO nanocomposites.

The elemental composition and chemical valence state of the F101@MoS<sub>2</sub>/ZnO composite were further analyzed by XPS measurements. In the full spectrum (Figures 2c and S3), the elements of C (1s, 284 eV), O (1s, 530 eV), Mo (3d, 229 eV), Fe (2p, 712.3 eV), S (2p, 161 eV), and Zn (2p, 1021 eV) can be readily identified. Based on the integrated peak areas, the sample was found to consist of 5.67 at % of Mo, 11.86 at % of S, 1.09 at % of Zn, 0.59 at % of Fe, and 42.37 at % of C (Table S1). In addition, the Mo/S atomic ratio was estimated to be 1:2.1, very close to the stoichiometric ratio of MoS<sub>2</sub>. In the high-resolution scan of the Mo 3d electrons (Figure 2d), deconvolution yields two doublets, where the first one at 229.2 and 232.3 eV can be assigned to the 3d<sub>5/2</sub> and 3d<sub>3/2</sub> electrons of Mo<sup>4+</sup> in 1T-MoS<sub>2</sub>, and the other at 233.6 and 236.5 eV to those of Mo<sup>6+</sup> of 2H-MoS<sub>2</sub> (the peak at 226.3 eV is due to the S 2s electrons of Mo-S in MoS<sub>2</sub>).<sup>46,47</sup> The S 2p spectrum of the F101@MoS<sub>2</sub>/ZnO composite is shown in Figure 2e, which can be deconvoluted into two peaks at 161.6 and 162.8 eV due to the 2p<sub>3/2</sub> and 2p<sub>1/2</sub> electrons of S in MoS<sub>2</sub>,<sup>42</sup> respectively. Figure 2f shows the corresponding Zn 2p spectrum, which includes a doublet at 1021.3 and 1044.6 eV arising from the Zn<sup>2+</sup> 2p<sub>3/2</sub> and Zn 2p<sub>1/2</sub> electrons of ZnO QDs. Consistent results were obtained with pristine MoS<sub>2</sub> (Figure S4) and F101@MoS<sub>2</sub> binary composite (Figure S5). Again, these results are consistent with the formation of ternary F101@MoS<sub>2</sub>/ZnO composite.

**3.2. Antibacterial Activity.** The antimicrobial activity of the MoS<sub>2</sub>, F101@MoS<sub>2</sub>, and F101@MoS<sub>2</sub>/ZnO nanocomposites was then evaluated and compared under visible light irradiation. From Figure 3a,c, one can see that a large number of *E. coli* and *S. aureus* cells grew on the agar medium in the dark, suggestive of minimal bactericidal activity of all samples without photoexcitation, yet under visible light irradiation (480–780 nm,  $0.36\text{ W cm}^{-2}$ ) for 30 min, the number of *E. coli* and *S. aureus* colonies decreased significantly, indicating high photodynamic activity in inhibiting bacterial growth, which also increased with increasing photoirradiation time (Figure S6). In particular, in the presence of the F101@MoS<sub>2</sub>/ZnO ternary composite, the bacteria barely grew on the plate medium, in comparison to MoS<sub>2</sub> and F101@MoS<sub>2</sub>, suggesting that F101@MoS<sub>2</sub>/ZnO stood out as the best among the sample series and ZnO played a critical role in dictating the bactericidal activity (Figure 3b,d). In fact, the antibacterial efficiency of MoS<sub>2</sub>, F101@MoS<sub>2</sub>, and F101@MoS<sub>2</sub>/ZnO composites against *E. coli* after 30 min visible irradiation was estimated to be 31.5, 63.4, and 98.6%, respectively (Figure 3b), whereas 15.2, 42.1, and 89.7% against *S. aureus* (Figure 3d). Notably, ICP-OES measurements showed that leaching of Zn<sup>2+</sup> ions from the F101@MoS<sub>2</sub>/ZnO composites into the aqueous solution under visible light irradiation was minimal, with a low concentration of  $0.92 \pm 0.12\text{ ppm}$  (Table S2), suggesting that the release of Zn<sup>2+</sup> ions was not the primary bactericidal effect.

Figure 4 shows the growth curves of (a) *E. coli* and (b) *S. aureus* in the presence of the F101@MoS<sub>2</sub>/ZnO composite at

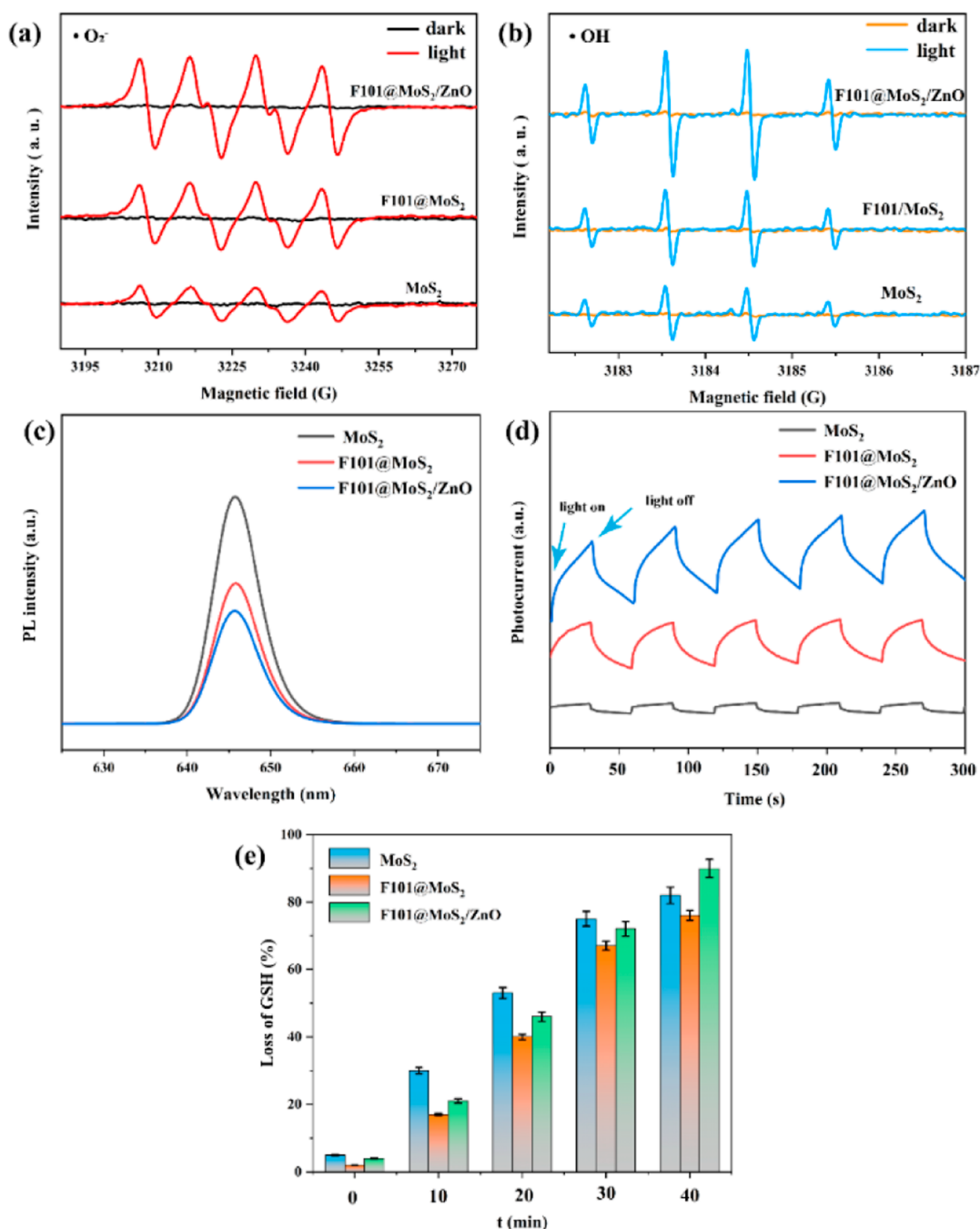


**Figure 6.** ESR spectra of the production of (a)  $\bullet\text{O}_2^-$  and (b)  $\bullet\text{OH}$  radicals under visible light radiation for 5 min with MoS<sub>2</sub>, F101@MoS<sub>2</sub>, and F101@MoS<sub>2</sub>/ZnO. (c) Photoluminescence emission spectra (the excitation wavelength 600 nm) and (d) photocurrent measurements of the sample series. (e) Ellman's assay of the loss of GSH after the treatment of the nanocomposite samples under visible light irradiation.

different concentrations in the dark, from which the MIC against *E. coli* and *S. aureus* can be estimated to be 0.4 and 0.6 mg mL<sup>-1</sup>, respectively. Additionally, one can see that the bacterial growth rate decreased with increasing concentration of the F101@MoS<sub>2</sub>/ZnO composite. The growth of bacteria colony ( $N$ ) is commonly modeled as a first-order reaction of time ( $t$ )

$$\frac{dN}{dt} = kN \quad (1)$$

with  $k$  being the first-order rate constant. Because the optical density of bacteria is proportional to the concentration,<sup>48</sup> this equation can be rearranged to

$$\ln\left(\frac{A}{A_0}\right) = kt \quad (2)$$

where  $A_0$  and  $A$  are the absorbance at 600 nm of the bacterial suspension at the starting time point and time  $t$ , respectively. From Figure 4c,d, the  $k$  values for both bacterial strands can be seen to decrease markedly with increasing composite concentration. For instance, in the absence of the nanocomposite (control measurements), the *E. coli* exhibited a



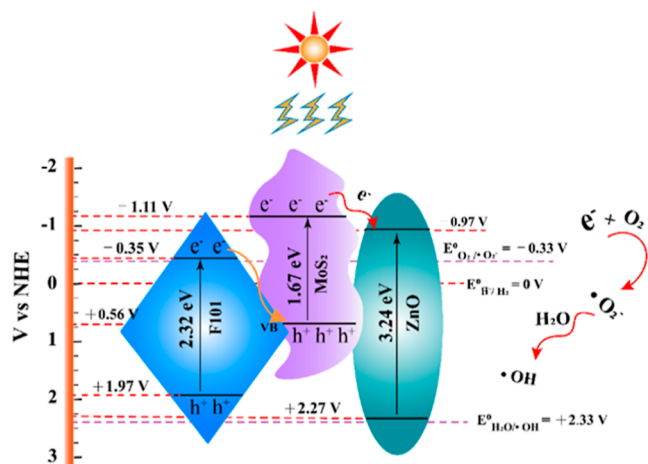


Figure 7. Electronic band structure of the ternary composite.

growth rate of  $1.67 \times 10^{-4} \text{ min}^{-1}$ , which decreased sharply by almost 2 orders of magnitude to only  $5.55 \times 10^{-6}$  with the addition of  $0.4 \text{ mg mL}^{-1}$  of the composites (Figure 4c). Similarly, for *S. aureus* (Figure 4d), the growth rate decreased drastically from  $1.14 \times 10^{-4}$  to  $8.56 \times 10^{-6} \text{ min}^{-1}$  before and after the addition of  $0.6 \text{ mg mL}^{-1}$  of the composites.

To validate the antibacterial activity of the F101@MoS<sub>2</sub>/ZnO composites, fluorescence staining with PI was employed to detect the living and dead bacteria. From the microscopic images in Figure 5a,b, the untreated *E. coli* and *S. aureus* can be seen to display a rod-like and spherical shape, respectively, along with strong green fluorescence, corresponding to a normal living state of the bacterial cells (Figure 5a1,b1). In contrast, almost all *E. coli* and *S. aureus* showed red fluorescence after visible light irradiation for 20 min in the presence of F101@MoS<sub>2</sub>/ZnO composite, suggesting effective damage of the bacteria cells (red fluorescence arises from the binding of PI to the DNA of damaged bacterial cells, Figure 5a2,b2). Such an evolution of the bacterial morphology can also be clearly seen in SEM measurements of *E. coli* (Figure 5c) and *S. aureus* (Figure 5e), where photoirradiative treatment with F101@MoS<sub>2</sub>/ZnO resulted in apparent damages of the bacterial cells (red arrows, Figure 5d,f).

**3.3. Antibacterial Mechanism.** To evaluate the contributions of radical species to the antimicrobial activity, ESR measurements were carried out with DMPO as the radical trap. From Figure 6a, it can be seen that no ESR signals were detected in the solution containing MoS<sub>2</sub>, F101@MoS<sub>2</sub>, or F101@MoS<sub>2</sub>/ZnO composites in the dark, yet after the exposure to visible light irradiation, apparent signals (quartets) emerged within the magnetic field strength of 3195 and 3255 G with  $g = 2.005$ , suggesting the formation of the superoxide radicals ( $\cdot\text{O}_2^-$ ),<sup>48</sup> and the peak-to-peak intensity can be seen to increase apparently in the order of MoS<sub>2</sub> < F101@MoS<sub>2</sub> < F101@MoS<sub>2</sub>/ZnO, indicating the high efficiency of  $\cdot\text{O}_2^-$  radical generation by the F101@MoS<sub>2</sub>/ZnO ternary composites as compared to the other two. Notably,  $\cdot\text{OH}$  species was also produced, as manifested by the quartet within the range of 3182 to 3186 G with  $g = 2.001$  (Figure 6b), and the F101@MoS<sub>2</sub>/ZnO composites exhibited a markedly higher  $\cdot\text{OH}$  yield than MoS<sub>2</sub> and F101@MoS<sub>2</sub>. This is likely due to the enhanced electron–hole separation of F101@MoS<sub>2</sub>/ZnO, in good agreement with the lowest photoluminescence emission among the sample series (Figure 6c).

Consistent results were obtained in photocurrent measurements. From Figure 6d, it can be seen that under visible light photoirradiation, the photocurrent increased in the order of MoS<sub>2</sub> < F101@MoS<sub>2</sub> < F101@MoS<sub>2</sub>/ZnO. This is also reflected in the photocatalytic degradation of methyl orange (Figure S7), where the degradation was completed in 120 min in the presence of the F101@MoS<sub>2</sub>/ZnO composite under visible light irradiation, where only ca. 80% was degraded by F101@MoS<sub>2</sub>.

Similar results were obtained in Ellman's assay. From Figure 6e, it can be seen that the loss of GSH increased with visible light radiation time in the presence of MoS<sub>2</sub>, F101@MoS<sub>2</sub>, and F101@MoS<sub>2</sub>/ZnO, and after 40 min photoirradiation, the loss reached 77, 84, and 87%, respectively, consistent with the highest efficiency of ROS generation by F101@MoS<sub>2</sub>/ZnO as manifested in ESR measurements.

Such a disparity of the photochemical activity can be accounted for by the electronic band structures of the ternary composites. From UV–vis absorption measurements (Figure S8), the effective band gap was estimated to be 1.67 eV for MoS<sub>2</sub>, 2.32 eV for F101, and 3.24 eV for ZnO, and the corresponding valence band maximum (VBM) was determined by XPS measurements (Figure S9) to be +0.56, +1.97, and +2.27 V (vs normal hydrogen electrode, NHE), with the conduction band minimum (CBM) at −1.11, −0.35, and −0.97 V.<sup>49</sup> One may notice that the VBMs are all less positive than the formal potential for water oxidation to  $\cdot\text{OH}$  (+2.33 V),<sup>48</sup> whereas the CBMs are all more negative than the formal potential for O<sub>2</sub> reduction to  $\cdot\text{O}_2^-$  (−0.33 V), as depicted in Figure 7. This suggests that  $\cdot\text{O}_2^-$  can be readily prepared by the reduction of O<sub>2</sub> by photogenerated electrons, whereas it is energetically difficult for the photogenerated holes to oxidize water to  $\cdot\text{OH}$ . Yet as both  $\cdot\text{O}_2^-$  and  $\cdot\text{OH}$  were clearly detected in ESR measurements, it suggests that  $\cdot\text{OH}$  was actually produced by the spontaneous disproportionation reaction of  $\cdot\text{O}_2^-$  with water,  $\cdot\text{O}_2^- + \text{H}_2\text{O} \rightarrow \text{O}_2 + \text{HO}_2^- + \cdot\text{OH}$ .<sup>50</sup>

For the binary F101@MoS<sub>2</sub> composite, the photogenerated carriers under visible irradiation (1.59–2.58 eV) likely followed the S-scheme charge-transfer mechanism, where the photoexcited electrons in the conduction band of the more reducing MoS<sub>2</sub> would transfer to the valence band of F101 (orange arrow, Figure 7), facilitating the charge separation and the formation of  $\cdot\text{O}_2^-$  and  $\cdot\text{OH}$  radicals.<sup>51</sup> For the ternary F101@MoS<sub>2</sub>/ZnO composite, the charge-separation efficiency was further enhanced by the formation of a p–n junction between MoS<sub>2</sub> and ZnO that boosted the interfacial charge transfer (red arrow, Figure 7) and ultimately the antimicrobial activity, as observed above—note that no photocarriers were generated for ZnO under visible photoirradiation because the band gap was too large.

## 4. CONCLUSIONS

In summary, F101@MoS<sub>2</sub>/ZnO ternary composites were successfully prepared by a facile hydrothermal approach, where ZnO QDs were grown onto the surface of the F101@MoS<sub>2</sub> scaffold and exhibited an excellent antimicrobial activity toward both Gram-negative and Gram-positive bacteria under visible light photoirradiation, as compared to MoS<sub>2</sub> and F101@MoS<sub>2</sub> binary composites. This was accounted for by the unique electronic band structure of the ternary composites that led to an enhanced efficiency in producing superoxide radicals by reduction of oxygen by photogenerated electrons. Hydroxy

radicals were then produced by disproportionation reaction of the superoxide radicals with water and responsible for the bactericidal actions, as confirmed in spectroscopic and microscopic measurements. Results from this study indicate that manipulation of the nanocomposite electronic band structure plays a critical role in dictating the charge separation efficiency, the formation of specific radical species, and the eventual photodynamic activity.

## ■ ASSOCIATED CONTENT

### SI Supporting Information

The Supporting Information is available free of charge at <https://pubs.acs.org/doi/10.1021/acsabm.2c00439>.

Elemental composition of the MoS<sub>2</sub>, F101@MoS<sub>2</sub>, and F101@MoS<sub>2</sub>/ZnO composites; dissolution of Zn<sup>2+</sup> ions from F101@MoS<sub>2</sub>/ZnO composites into aqueous solutions; zeta potentials of F101, MoS<sub>2</sub>, F101@MoS<sub>2</sub>, and F101@MoS<sub>2</sub>/ZnO in water; TEM images of MoS<sub>2</sub> nanosheets, ZnO QDs, and F101@MoS<sub>2</sub>/ZnO; zoom-in of the XPS full spectrum of F101@MoS<sub>2</sub>/ZnO and high-resolution scans of Fe 2p of F101@MoS<sub>2</sub>/ZnO; XPS full spectrum of MoS<sub>2</sub> and F101@MoS<sub>2</sub> and high-resolution scans of C 1s, Mo 3d, and S 2p electrons of MoS<sub>2</sub>; photographs of the growth of *E. coli* and *S. aureus* under visible irradiation; visible-light photocatalytic degradation of methyl orange and corresponding degradation efficiency; UV-Vis absorption spectra of MoS<sub>2</sub>, F101, ZnO, and F101@MoS<sub>2</sub>/ZnO and the corresponding Tauc plots; and valence-band XPS spectra of F101, MoS<sub>2</sub>, and ZnO QDs (PDF)

## ■ AUTHOR INFORMATION

### Corresponding Authors

**Junli Liu** – School of Materials and Engineering, Shaanxi Key Laboratory of Green Preparation and Functionalization for Inorganic Materials, Shaanxi University of Science & Technology, Xi'an, Shaanxi 710021, China; [orcid.org/0000-0003-0699-4619](https://orcid.org/0000-0003-0699-4619); Email: [liujunli042@163.com](mailto:liujunli042@163.com)

**Shaowei Chen** – Department of Chemistry and Biochemistry, University of California, Santa Cruz, California 96064, United States; [orcid.org/0000-0002-3668-8551](https://orcid.org/0000-0002-3668-8551); Email: [shaowei@ucsc.edu](mailto:shaowei@ucsc.edu)

### Authors

**Wenxia Cheng** – School of Materials and Engineering, Shaanxi Key Laboratory of Green Preparation and Functionalization for Inorganic Materials, Shaanxi University of Science & Technology, Xi'an, Shaanxi 710021, China

**Kaitao Zhang** – School of Materials and Engineering, Shaanxi Key Laboratory of Green Preparation and Functionalization for Inorganic Materials, Shaanxi University of Science & Technology, Xi'an, Shaanxi 710021, China

**Hui Liu** – School of Materials and Engineering, Shaanxi Key Laboratory of Green Preparation and Functionalization for Inorganic Materials, Shaanxi University of Science & Technology, Xi'an, Shaanxi 710021, China; [orcid.org/0000-0002-5966-1191](https://orcid.org/0000-0002-5966-1191)

**Junqi Li** – School of Materials and Engineering, Shaanxi Key Laboratory of Green Preparation and Functionalization for Inorganic Materials, Shaanxi University of Science & Technology, Xi'an, Shaanxi 710021, China

**John Tressel** – Department of Chemistry and Biochemistry, University of California, Santa Cruz, California 96064, United States

Complete contact information is available at: <https://pubs.acs.org/doi/10.1021/acsabm.2c00439>

### Author Contributions

The manuscript was written through contributions of all authors. All authors have given approval to the final version of the manuscript.

### Notes

The authors declare no competing financial interest.

## ■ ACKNOWLEDGMENTS

This work was supported by the National Natural Science Foundation of China for Young Scholars (51802185), the National Key R&D Program of China (2019YFC1520100), and the Shaanxi Province Innovation Ability Support Plan-Youth Science and Technology New Stars (S2020-ZC-XXXM-0081). S.W.C. thanks the National Science Foundation (CBET-1848841) for partial support of the work.

## ■ REFERENCES

- (1) Seltnerich, N. Unwell: The Public Health Implications of Unregulated Drinking Water. *Environ. Health Perspect.* **2017**, *125*, 114001.
- (2) Morgan, C.; Bowling, M.; Bartram, J.; Lyn Kayser, G. Water, sanitation, and hygiene in schools: Status and implications of low coverage in Ethiopia, Kenya, Mozambique, Rwanda, Uganda, and Zambia. *Int. J. Hyg Environ. Health* **2017**, *220*, 950–959.
- (3) Li, S.; Dong, S.; Xu, W.; Tu, S.; Yan, L.; Zhao, C.; Ding, J.; Chen, X. Antibacterial Hydrogels. *Adv. Sci.* **2018**, *5*, 1700527.
- (4) MacVane, S. H.; Pharm, D. Antimicrobial Resistance in the Intensive Care Unit: A Focus on Gram-Negative Bacterial Infections. *J. Intensive Care Med.* **2017**, *32*, 25–37.
- (5) Santevecchi, B. A.; Smith, T. T.; MacVane, S. H. Clinical experience with ceftazidime/avibactam for treatment of antibiotic-resistant organisms other than *Klebsiella pneumoniae*. *Int. J. Antimicrob. Agents* **2018**, *51*, 629–635.
- (6) Hook, A. L.; Chang, C. Y.; Yang, J.; Atkinson, S.; Langer, R.; Anderson, D. G.; Davies, M. C.; Williams, P.; Alexander, M. R. Discovery of novel materials with broad resistance to bacterial attachment using combinatorial polymer microarrays. *Adv. Mater.* **2013**, *25*, 2542–2547.
- (7) Hu, D.; Li, H.; Wang, B.; Ye, Z.; Lei, W.; Jia, F.; Jin, Q.; Ren, K. F.; Ji, J. Surface-Adaptive Gold Nanoparticles with Effective Adherence and Enhanced Photothermal Ablation of Methicillin-Resistant *Staphylococcus aureus* Biofilm. *ACS Nano* **2017**, *11*, 9330–9339.
- (8) Zhang, R.; Xing, R.; Jiao, T.; Ma, K.; Chen, C.; Ma, G.; Yan, X. Carrier-Free, Chemophotodynamic Dual Nanodrugs via Self-Assembly for Synergistic Antitumor Therapy. *ACS Appl. Mater. Interfaces* **2016**, *8*, 13262–13269.
- (9) Li, Y.; Liu, X.; Tan, L.; Cui, Z.; Yang, X.; Zheng, Y.; Yeung, K. W. K.; Chu, P. K.; Wu, S. Rapid Sterilization and Accelerated Wound Healing Using Zn<sup>2+</sup> and Graphene Oxide Modified g-C<sub>3</sub>N<sub>4</sub> under Dual Light Irradiation. *Adv. Funct. Mater.* **2018**, *28*, 1800299.
- (10) Wei, T.; Yu, Q.; Chen, H. Responsive and Synergistic Antibacterial Coatings: Fighting against Bacteria in a Smart and Effective Way. *Adv. Healthcare Mater.* **2019**, *8*, e1801381.
- (11) Melamed, J. R.; Edelstein, R. S.; Day, E. S. Elucidating the Fundamental Mechanisms of Cell Death Triggered by Photothermal Therapy. *ACS Nano* **2015**, *9*, 6–11.
- (12) Mao, C.; Xiang, Y.; Liu, X.; Cui, Z.; Yang, X.; Yeung, K. W. K.; Pan, H.; Wang, X.; Chu, P. K.; Wu, S. Photo-Inspired Antibacterial Activity and Wound Healing Acceleration by Hydrogel Embedded

- with Ag/Ag@AgCl/ZnO Nanostructures. *ACS Nano* **2017**, *11*, 9010–9021.
- (13) Tan, L.; Li, J.; Liu, X.; Cui, Z.; Yang, X.; Zhu, S.; Li, Z.; Yuan, X.; Zheng, Y.; Yeung, K. W. K.; Pan, H.; Wang, X.; Wu, S. Rapid Biofilm Eradication on Bone Implants Using Red Phosphorus and Near-Infrared Light. *Adv. Mater.* **2018**, *30*, e1801808.
- (14) Zhang, X.; Zhang, G.; Zhang, H.; Liu, X.; Shi, J.; Shi, H.; Yao, X.; Chu, P. K.; Zhang, X. A bifunctional hydrogel incorporated with CuS@MoS<sub>2</sub> microspheres for disinfection and improved wound healing. *Chem. Eng. J.* **2020**, *382*, 122849.
- (15) Tan, L.; Li, J.; Liu, X.; Cui, Z.; Yang, X.; Yeung, K. W. K.; Pan, H.; Zheng, Y.; Wang, X.; Wu, S. In Situ Disinfection through Photoinspired Radical Oxygen Species Storage and Thermal-Triggered Release from Black Phosphorous with Strengthened Chemical Stability. *Small* **2018**, *14*, 1703197.
- (16) Meng, F.; Li, J.; Cushing, S. K.; Zhi, M.; Wu, N. Solar hydrogen generation by nanoscale p-n junction of p-type molybdenum disulfide/n-type nitrogen-doped reduced graphene oxide. *J. Am. Chem. Soc.* **2013**, *135*, 10286–10289.
- (17) Feng, Z.; Liu, X.; Tan, L.; Cui, Z.; Yang, X.; Li, Z.; Zheng, Y.; Yeung, K. W. K.; Wu, S. Electrophoretic Deposited Stable Chitosan@MoS<sub>2</sub> Coating with Rapid In Situ Bacteria-Killing Ability under Dual-Light Irradiation. *Small* **2018**, *14*, 1704347.
- (18) Liu, W.; Feng, Y.; Tang, H.; Yuan, H.; He, S.; Miao, S. Immobilization of silver nanocrystals on carbon nanotubes using ultra-thin molybdenum sulfide sacrificial layers for antibacterial photocatalysis in visible light. *Carbon* **2016**, *96*, 303–310.
- (19) Zheng, L.; Han, S.; Liu, H.; Yu, P.; Fang, X. Hierarchical MoS<sub>2</sub> Nanosheet@TiO<sub>2</sub> Nanotube Array Composites with Enhanced Photocatalytic and Photocurrent Performances. *Small* **2016**, *12*, 1527–1536.
- (20) Guo, Z.; Chen, Z.; Shi, Z.; Qian, J.; Li, J.; Mei, T.; Wang, J.; Wang, X.; Shen, P. Stable metallic 1T phase engineering of molybdenum disulfide for enhanced solar vapor generation. *Sol. Energy Mater. Sol. Cells* **2020**, *204*, 110227.
- (21) Wang, S.; Li, X.; Chen, Y.; Cai, X.; Yao, H.; Gao, W.; Zheng, Y.; An, X.; Shi, J.; Chen, H. A Facile One-Pot Synthesis of a Two-Dimensional MoS<sub>2</sub>/Bi<sub>2</sub>S<sub>3</sub> Composite Theranostic Nanosystem for Multi-Modality Tumor Imaging and Therapy. *Adv. Mater.* **2015**, *27*, 2775–2782.
- (22) Zhu, C.; Zeng, Z.; Li, H.; Li, F.; Fan, C.; Zhang, H. Single-layer MoS<sub>2</sub>-based nanopores for homogeneous detection of biomolecules. *J. Am. Chem. Soc.* **2013**, *135*, 5998–6001.
- (23) Yu, J.; Zhuang, S.; Xu, X.; Zhu, W.; Feng, B.; Hu, J. Photogenerated electron reservoir in hetero-p-n CuO–ZnO nanocomposite device for visible-light-driven photocatalytic reduction of aqueous Cr(vi). *J. Mater. Chem. A* **2015**, *3*, 1199–1207.
- (24) Dong, C.; Xiao, X.; Chen, G.; Guan, H.; Wang, Y. Synthesis and photocatalytic degradation of methylene blue over p-n junction Co<sub>3</sub>O<sub>4</sub>/ZnO core/shell nanorods. *Mater. Chem. Phys.* **2015**, *155*, 1–8.
- (25) Jiang, J.; Zhang, X.; Sun, P.; Zhang, L. ZnO/BiOI Heterostructures: Photoinduced Charge-Transfer Property and Enhanced Visible-Light Photocatalytic Activity. *J. Phys. Chem. C* **2011**, *115*, 20555–20564.
- (26) Kudo, A.; Miseki, Y. Heterogeneous photocatalyst materials for water splitting. *Chem. Soc. Rev.* **2009**, *38*, 253–278.
- (27) Chan, S. H. S.; Yeong Wu, T.; Juan, J. C.; Teh, C. Y. Recent developments of metal oxide semiconductors as photocatalysts in advanced oxidation processes (AOPs) for treatment of dye wastewater. *J. Chem. Technol. Biotechnol.* **2011**, *86*, 1130–1158.
- (28) Ong, C. B.; Ng, L. Y.; Mohammad, A. W. A review of ZnO nanoparticles as solar photocatalysts: Synthesis, mechanisms and applications. *Renew. Sustain. Energy Rev.* **2018**, *81*, 536–551.
- (29) Wu, D.; Wang, Y.; Ma, N.; Cao, K.; Zhang, W.; Chen, J.; Wang, D.; Gao, Z.; Xu, F.; Jiang, K. Single-crystal-like ZnO mesoporous spheres derived from metal organic framework delivering high electron mobility for enhanced energy conversion and storage performances. *Electrochim. Acta* **2019**, *305*, 474–483.
- (30) Yao, P.; Liu, H.; Wang, D.; Chen, J.; Li, G.; An, T. Enhanced visible-light photocatalytic activity to volatile organic compounds degradation and deactivation resistance mechanism of titania confined inside a metal-organic framework. *J. Colloid Interface Sci.* **2018**, *522*, 174–182.
- (31) Zhang, Z.; Li, X.; Liu, B.; Zhao, Q.; Chen, G. Hexagonal microspindle of NH<sub>2</sub>-MIL-101(Fe) metal–organic frameworks with visible-light-induced photocatalytic activity for the degradation of toluene. *RSC Adv.* **2016**, *6*, 4289–4295.
- (32) Karthik, P.; Vinoth, R.; Zhang, P.; Choi, W.; Balaraman, E.; Neppolian, B.  $\pi$ - $\pi$  Interaction Between Metal–Organic Framework and Reduced Graphene Oxide for Visible-Light Photocatalytic H<sub>2</sub> Production. *ACS Appl. Energy Mater.* **2018**, *1*, 1913–1923.
- (33) Almási, M.; Zelenák, V.; Palotai, P.; Beňová, E.; Zelenáková, A. Metal-organic framework MIL-101(Fe)-NH<sub>2</sub> functionalized with different long-chain polyamines as drug delivery system. *Inorg. Chem. Commun.* **2018**, *93*, 115–120.
- (34) Zhang, Y.; Wang, F.; Ju, E.; Liu, Z.; Chen, Z.; Ren, J.; Qu, X. Metal-Organic-Framework-Based Vaccine Platforms for Enhanced Systemic Immune and Memory Response. *Adv. Funct. Mater.* **2016**, *26*, 6454–6461.
- (35) Su, S.; Xing, Z.; Zhang, S.; Du, M.; Wang, Y.; Li, Z.; Chen, P.; Zhu, Q.; Zhou, W. Ultrathin mesoporous g-C<sub>3</sub>N<sub>4</sub>/NH<sub>2</sub>-MIL-101(Fe) octahedron heterojunctions as efficient photo-Fenton-like system for enhanced photo-thermal effect and promoted visible-light-driven photocatalytic performance. *Appl. Surf. Sci.* **2021**, *537*, 147890.
- (36) Song, Y.; He, L.; Zhang, S.; Liu, X.; Chen, K.; Jia, Q.; Zhang, Z.; Du, M. Novel impedimetric sensing strategy for detecting ochratoxin A based on NH<sub>2</sub>-MIL-101(Fe) metal-organic framework doped with cobalt phthalocyanine nanoparticles. *Food Chem.* **2021**, *351*, 129248.
- (37) Zou, X.; Zhang, J.; Zhao, X.; Zhang, Z. MoS<sub>2</sub>/RGO composites for photocatalytic degradation of ranitidine and elimination of NDMA formation potential under visible light. *Chem. Eng. J.* **2020**, *383*, 123084.
- (38) Wang, X.; Li, J. Sol-gel fabrication of Ag-Coated ZnO quantum dots nanocomposites with excellent photocatalytic activity. *Opt. Mater.* **2021**, *118*, 111235.
- (39) Dong, Y.; Hu, T.; Pudukudy, M.; Su, H.; Jiang, L.; Shan, S.; Jia, Q. Influence of microwave-assisted synthesis on the structural and textural properties of mesoporous MIL-101(Fe) and NH<sub>2</sub>-MIL-101(Fe) for enhanced tetracycline adsorption. *Mater. Chem. Phys.* **2020**, *251*, 123060.
- (40) Dao, X.-Y.; Xie, X.-F.; Guo, J.-H.; Zhang, X.-Y.; Kang, Y.-S.; Sun, W.-Y. Boosting Photocatalytic CO<sub>2</sub> Reduction Efficiency by Heterostructures of NH<sub>2</sub>-MIL-101(Fe)/g-C<sub>3</sub>N<sub>4</sub>. *ACS Appl. Energy Mater.* **2020**, *3*, 3946–3954.
- (41) Zhu, M.; Liu, X.; Tan, L.; Cui, Z.; Liang, Y.; Li, Z.; Kwok Yeung, K. W.; Wu, S. Photo-responsive chitosan/Ag/MoS<sub>2</sub> for rapid bacteria-killing. *J. Hazard. Mater.* **2020**, *383*, 121122.
- (42) Wang, D.; Zhang, X.; Bao, S.; Zhang, Z.; Fei, H.; Wu, Z. Phase engineering of a multiphasic 1T/2H MoS<sub>2</sub> catalyst for highly efficient hydrogen evolution. *J. Mater. Chem. A* **2017**, *5*, 2681–2688.
- (43) Voiry, D.; Mohite, A.; Chhowalla, M. Phase engineering of transition metal dichalcogenides. *Chem. Soc. Rev.* **2015**, *44*, 2702–2712.
- (44) Schindler, T.; Lin, W.; Schmutzler, T.; Lindner, P.; Peukert, W.; Segets, D.; Unruh, T. Evolution of the Ligand Shell Around Small ZnO Nanoparticles During the Exchange of Acetate by Catechol: A Small Angle Scattering Study. *ChemNanoMat* **2018**, *5*, 116–123.
- (45) Singh, P.; Singh, R. K.; Kumar, R. Journey of ZnO quantum dots from undoped to rare-earth and transition metal-doped and their applications. *RSC Adv.* **2021**, *11*, 2512–2545.
- (46) Manikandan, A.; Ilango, P. R.; Chen, C.-W.; Wang, Y.-C.; Shih, Y.-C.; Lee, L.; Wang, Z. M.; Ko, H.; Chueh, Y.-L. Superior dye adsorbent towards the hydrogen evolution reaction combining active sites and phase-engineering of (1T/2H) MoS<sub>2</sub>/ $\alpha$ -MoO<sub>3</sub> hybrid heterostructured nanoflowers. *J. Mater. Chem. A* **2018**, *6*, 15320–15329.



(47) Chang, K.; Hai, X.; Pang, H.; Zhang, H.; Shi, L.; Liu, G.; Liu, H.; Zhao, G.; Li, M.; Ye, J. Targeted Synthesis of 2H- and 1T-Phase MoS<sub>2</sub> Monolayers for Catalytic Hydrogen Evolution. *Adv. Mater.* **2016**, *28*, 10033–10041.

(48) Chata, G.; Nichols, F.; Mercado, R.; Assafa, T.; Millhauser, G. L.; Saltikov, C.; Chen, S. Photodynamic Activity of Graphene Oxide/Polyaniline/Manganese Oxide Ternary Composites toward Both Gram-Positive and Gram-Negative Bacteria. *ACS Appl. Bio Mater.* **2021**, *4*, 7025–7033.

(49) Yan, M.; Hua, Y.; Zhu, F.; Sun, L.; Gu, W.; Shi, W. Constructing nitrogen doped graphene quantum dots-ZnNb<sub>2</sub>O<sub>6</sub>/g-C<sub>3</sub>N<sub>4</sub> catalysts for hydrogen production under visible light. *Appl. Catal., B* **2017**, *206*, 531–537.

(50) Nichols, F.; Ozoemena, K. I.; Chen, S. W. Electrocatalytic Generation of Reactive Species and Implications in Microbial Inactivation. *Chin. J. Catal.* **2022**, *43*, 1399–1416.

(51) Xu, Q. L.; Zhang, L. Y.; Cheng, B.; Fan, J. J.; Yu, J. G. S-Scheme Heterojunction Photocatalyst. *Chem* **2020**, *6*, 1543–1559.

## Recommended by ACS

### Enhanced Antifungal Activity of WS<sub>2</sub>/ZnO Nanohybrid against *Candida albicans*

Vidhi K. Bhatt, Dattatray J. Late, *et al.*

SEPTEMBER 28, 2020  
ACS BIOMATERIALS SCIENCE & ENGINEERING

READ 

### Laser-Induced MoO<sub>x</sub>/Sulfur-Doped Graphene Hybrid Frameworks as Efficient Antibacterial Agents

Yong Yang, Yafei Zhang, *et al.*

JANUARY 22, 2021  
LANGMUIR

READ 

### Gold Nanoclusters-Coated Orthodontic Devices Can Inhibit the Formation of *Streptococcus mutans* Biofilm

Yangzhouyun Xie, Xingyu Jiang, *et al.*

JANUARY 07, 2020  
ACS BIOMATERIALS SCIENCE & ENGINEERING

READ 

### Anti-quorum Sensing and Anti-biofilm Activity of Zinc Oxide Nanospikes

Mohd. Farhan Khan, Iqbal Ahmad, *et al.*

DECEMBER 10, 2020  
ACS OMEGA

READ 

Get More Suggestions >